Deep-inelastic scattering in ^{124,136}Xe+^{58,64}Ni at energies near the Coulomb barrier

J. Gehring,[1,2] B. B. Back,[1] K. C. Chan,[1] M. Freer,[1] D. Henderson,[1] C. L. Jiang,[1] K. E. Rehm,[1] J. P. Schiffer,[1,2] M. Wolanski,[1,2] and A. H. Wuosmaa[1]

[1]*Argonne National Laboratory, Argonne, Illinois 60439*

[2]*University of Chicago, Chicago, Illinois 60637*

(Received 19 August 1996)

Cross sections, angular distributions, and mass distributions have been measured for deep-inelastic scattering in ^{124}Xe+^{58}Ni and ^{136}Xe+^{64}Ni at laboratory energies in the vicinity of the Coulomb barrier. The mass distributions show distinct components due to deep-inelastic and fissionlike processes. The strength of deep-inelastic scattering is similar in the two systems measured and comparable to previous measurements in ^{58}Ni+^{112,124}Sn. [S0556-2813(97)04306-9]

PACS number(s): 25.70.−z

I. INTRODUCTION

During the last 15 years, considerable effort has been devoted to understanding the fusion of heavy nuclei at energies near or below the Coulomb barrier. Reasonable agreement of theory with the experimental results has been achieved in many cases by including the coupling of low-lying excited states of the projectile and target in the calculation of the fusion cross sections. In the vicinity of the Coulomb barrier, various reaction modes occurring in the interaction of two heavy ions are thus known to strongly influence each other and the most studied of these connections is the effect of quasielastic processes (inelastic scattering and transfer) on the fusion probability.

Little information is available about competition with other processes, such as deep-inelastic scattering [1–3]. Most studies of deep-inelastic scattering have been performed at energies above the barrier where various damping mechanisms are normally invoked to explain the loss of kinetic energy in this process. It was therefore a surprise when the systems ^{58}Ni+^{112,124}Sn were found to exhibit many of the features of deep-inelastic scattering at near or subbarrier energies [4]. The kinetic energy of the reaction products in both systems was smaller than the barrier energy by 40–50 MeV, the smallest observed energy being relatively independent of the bombarding energy. These deep-inelastic processes were found to be an important reaction mode, contributing 8–10 % of the total reaction cross section at energies below the barrier.

The experiments of Wolfs [4] involved nuclei with a closed proton shell for both projectile, Ni, and target, Sn. In this paper, results are presented of similar measurements involving a closed neutron shell ^{136}Xe and a transitional nucleus ^{124}Xe, incident on targets of ^{58}Ni and ^{64}Ni, respectively, in order to study whether a similar nuclear structure dependence as observed in subbarrier fusion reactions [5] can also be found in subbarrier deep-inelastic processes. In order to improve the detection efficiency for the experiments, the reactions were studied by using inverse kinematics, i.e., bombarding lighter targets ^{58,64}Ni with heavier beams ^{124,136}Xe.

II. EXPERIMENTAL METHOD

The measurements were performed using the ATLAS accelerator at the Argonne National Laboratory. Beams of ^{124,136}Xe ions of energy 522–556 MeV were incident on 98%-enriched ^{58,64}Ni, targets of thickness 50–400 μg/cm^2. The targets were mounted in the center of a 90-cm-diam scattering chamber. Two extension boxes were mounted on adjacent sides of the chamber, separated by 45°. The walls of the chamber and the extension boxes were connected to the base by a rotating vacuum seal and could be rotated by up to $\pm 25°$ with respect to the targets and beam line. The beam was collimated to 3 mm diameter by two Ta apertures located 30 and 45 cm upstream of the target.

The reaction products were detected in kinematic coincidence in three large-area, position-sensitive parallel grid avalanche counters (PGAC). The counters were all of the parallel-grid type described in detail in Ref. [6]. A fast time signal derived from the anode grid was used for time-of-flight (TOF) measurements relative to the rf signal from the accelerator. The position in two dimensions was obtained by a delay line readout. The time and position resolution were 400 psec and 1.5 mm, respectively. The absence of cathode and anode foils in the parallel-grid detector reduced the amount of material traversed by incident heavy ions and decreased the detection energy threshold. The entrance foils on all detectors were 1-μm-thick Mylar which allowed the detection of Xe ions with a kinetic energy of as little as 10 MeV.

Two of the counters were mounted inside the two extension boxes. The third counter was fixed to the chamber in the ^{136}Xe measurements and mounted on a rotating platform in the ^{134}Xe measurements. The latter arrangement proved more advantageous as it allowed rotation of the third detector with respect to the first two. The first two counters had active areas 45 cm in length and 10 cm in height [6]. They were located at a distance of 115 cm from the target to the anode grid of the counter. The third had an active area 20 cm in length and 20 cm in height [4]. It was located at a distance of 56 cm from the target to the anode grid in the ^{136}Xe experiment and a distance of 32 cm from the target to the anode grid in the ^{124}Xe experiment. The experimental setup is illustrated in Fig. 1.

The absolute TOF as well as the relative time difference

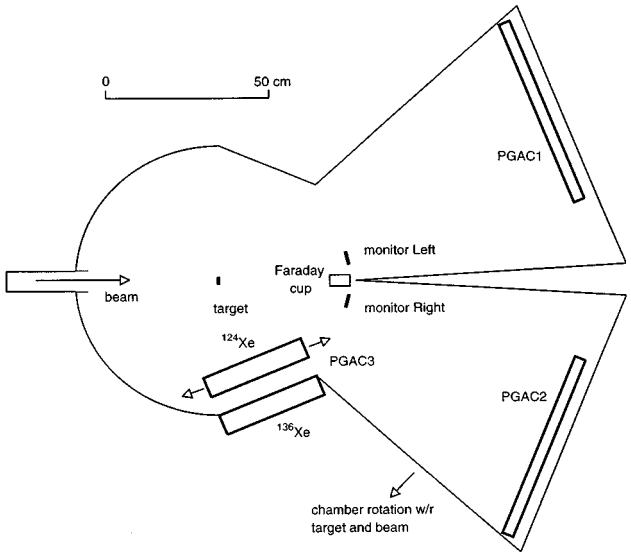

FIG. 1. Schematic diagram of the experimental arrangement. PGAC3 was fixed to the outside of the chamber in the ^{136}Xe measurements and was located inside the chamber to allow rotation with respect to 1 and 2 in the ^{124}Xe measurements. The chamber could be rotated by $\pm 25°$ with respect to the beam and target, the zero angle being that which placed PGAC1 directly behind the beam.

and position of the incident particles was measured for kinematic coincidences between the detector pairs 1-2 and 1-3. The data were corrected for energy loss in the target material, deviations in the direction of the beam, and the propagation time of the signal across the anode wire planes of the detectors. The corrections were less than 0.1° in the measured angles and 3 nsec in the measured TOF's. The masses, c.m. scattering angle, and Q value for the reaction products were then calculated from the measured parameters, assuming two-body kinematics. Events arising from nonbinary reactions or random coincidences between detectors were rejected through examination of the sum of the azimuthal angles. The mass resolution was typically 1 u full width at half maximum (FWHM) and the energy resolution 5 MeV. Events resulting from impurities in either target or beam were removed from the data by comparison of the final state masses calculated using the absolute TOF and the relative time difference. This was possible because the six measured parameters overdetermine the reaction kinematics for two-body events.

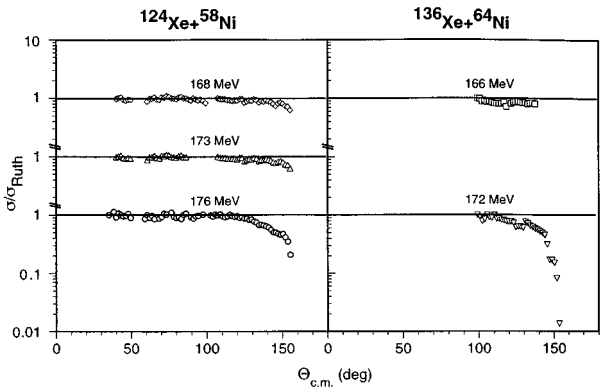

FIG. 2. Ratio of the measured elastic plus quasielastic scattering cross section to the Rutherford cross section is shown for ^{124}Xe $+ ^{58}$Ni and ^{136}Xe$+ ^{64}$Ni. The data are labeled by the center-of-mass energy.

The elastic scattering of the beam from the target was measured at laboratory angles forward of 10° by a pair of Si surface barrier detectors. This information was used to provide a relative normalization between runs. The absolute normalization was determined from a comparison of the elastic scattering cross section measured with the PGAC's at forward angles to the Rutherford value.

The bombarding energy was measured from the TOF of a beam bunch between three different resonator pairs in the ATLAS Linac [7], with a typical uncertainty of 0.5 MeV. The beam energies were corrected for the loss in the carbon backings of the targets, which faced the beam, and in half of the Ni material, using the systematics of Anderson and Ziegler [8]. The uncertainty in this correction is taken to be one-half of its total magnitude. The relevant beam and target parameters are listed in Table I.

III. RESULTS

A. Elastic+quasielastic scattering

The ratio of the measured elastic+quasielastic scattering cross sections to the Rutherford cross section is shown in Fig. 2 for both systems and all bombarding energies. In these cross sections all events with Q values greater than -20 MeV were included, as the resolution did not allow the separation of elastic scattering from quasielastic reactions.

As the elastic+quasielastic angular distributions do not extend backwards of the quarter-point angle ($\sigma/\sigma_R = 1/4$), it

TABLE I. Reaction parameters.

Projectile	E_{lab} (MeV)	^{12}C (μg/cm^2)	Ni (μg/cm^2)	$(E_{lab}-\Delta E)$[a] (MeV)	$E_{c.m.}$ (MeV)	E/B[b]
^{124}Xe	556.2±0.5	20	56	553.6±1.4	176.4±0.4	1.005(3)
^{124}Xe	544.6±0.5	20	56	542.0±1.4	172.7±0.4	0.984(2)
^{124}Xe	529.2±0.5	20	56	526.7±1.4	167.8±0.4	0.956(2)
^{136}Xe	545.9±0.5	0	397	539±4	172.4±1.1	1.013(7)
^{136}Xe	522.1±0.5	20	78	519.4±1.4	166.2±0.5	0.977(3)

[a] ΔE = energy loss in C and 1/2 of Ni target (see text).
[b] Calculated using $r_0 = 1.4$ fm.

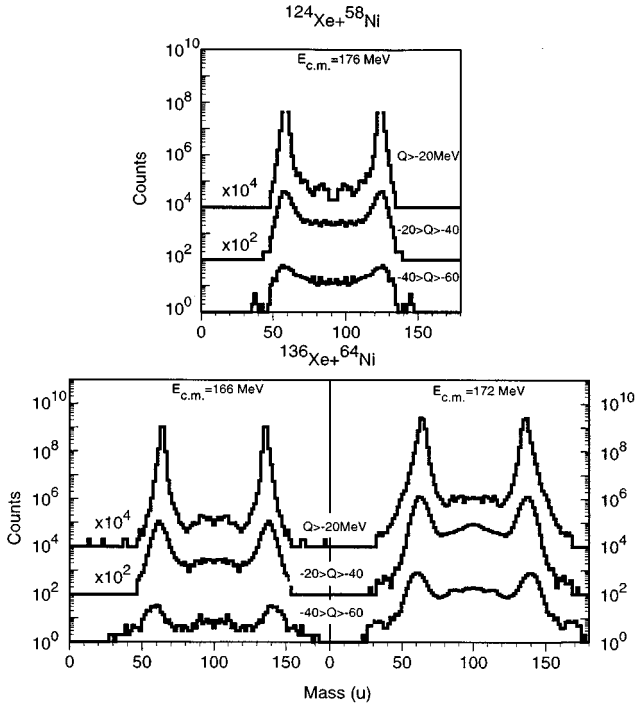

FIG. 3. Mass distributions for the two systems studied for different ranges of Q value.

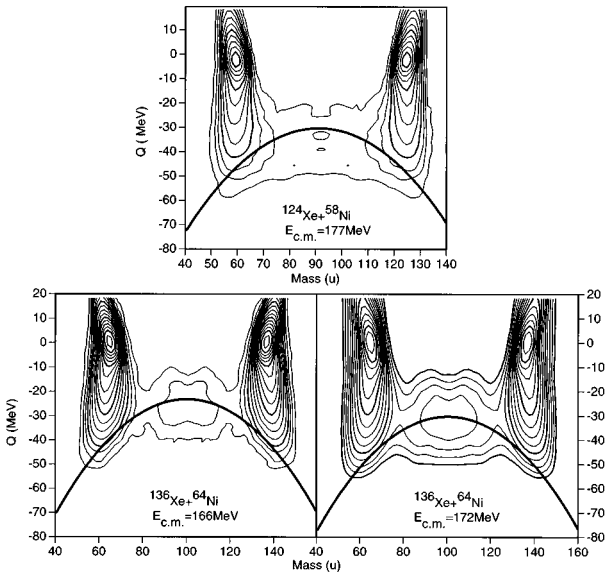

FIG. 4. Contour plots of the yield as a function of mass and Q value, with a logarithmic scale, such that four contours represent a factor of 10. The solid lines represent the Viola systematics as described in the text.

was not possible to extract the total reaction cross sections from the experimental data.

B. Mass distributions

Mass distributions are shown for a subset of the data in Fig. 3. The distributions exhibit two components. The first component is sharply peaked around the masses of projectile and target, with the peak becoming broader at more negative Q values. The second component exhibits a rather broader peak centered at half of the mass of the composite system.

Contour diagrams of the cross section versus mass and Q value are shown in Fig. 4. The solid curves represent the average Q value expected on the basis of the Viola systematics [9] for the total kinetic energy E_K in fissionlike processes. The Viola systematics represents the Coulomb repulsion for an elongated scission configuration where the charge centers are approximately 50% farther apart than for a touching sphere configuration. The solid curves are thus given by

$$Q = E_K - E_{\text{c.m.}} = 0.787\left(\frac{Z_1 Z_2}{A_1^{1/3} + A_2^{1/3}}\right) - E_{\text{c.m.}}$$

$$= 0.787\left(\frac{Z}{A}\right)^2\left(\frac{A_1 A_2}{A_1^{1/3} + A_2^{1/3}}\right) - E_{\text{c.m.}} \ \text{(MeV)},$$

where the charge and mass numbers of the combined system and the individual fragments are denoted by Z, Z_1, Z_2 and A, A_1, A_2, respectively, and it is assumed that the system is charge equilibrated at scission. We observe that the fissionlike products essentially follow this curve and, furthermore, that the quasielastic and deep-inelastic processes extend from elastic scattering at $Q = 0$ to the fully damped value consistent with the fissionlike kinetic energies. At these energies the two reaction types blend into each other and become indistinguishable. Although the center-of-mass energy in the entrance channel is already very close to the barrier, we see that deep-inelastic fragments can emerge with lower kinetic energies by reaching very elongated shapes before reseparating.

For the most negative Q values, the ^{136}Xe data exhibit a drift toward larger mass asymmetry, an effect that is less clear in the ^{124}Xe data. This can be understood in terms of the potential energy surface for touching spheres as given by the liquid drop model which show a strong driving potential for mass transfer in the ^{136}Xe case and a weaker driving force for ^{124}Xe.

The tails of the Q-value distribution toward the unphysical positive values are the result of energy loss and small-angle scattering in the target material. This was verified by Monte Carlo calculations including these effects. The results of the calculations are shown in Fig. 5(a). The calculations are based on an initial energy of $E_{\text{lab}} = 556$ MeV for ^{124}Xe $+ ^{58}$Ni, a target thickness of 60 μg/cm^2, and an initial distribution in mass and Q, which is a delta function around the projectile mass and $Q = -50$ MeV. These initial values are chosen as they are typical of the experimental data (see Figs. 3, 4, and 6) and allow a comparison of target effects with those of neutron evaporation, which are significant at the more negative Q values. The same calculation including neutron evaporation is shown in Fig. 5(b). The neutron multiplicity and energy spectrum are obtained from the statistical model using PACE code [10] calculations for fusion reactions leading to nuclei with similar excitation energies and angular momenta as the deep-inelastic products. Neutron evaporation is seen to move the distribution toward lower masses and more negative Q values and to introduce a considerable broadening in both mass and Q.

C. Total kinetic energies

Spectra of the total kinetic energy (TKE) of reaction products with a mass within 10 u of projectile or target are shown

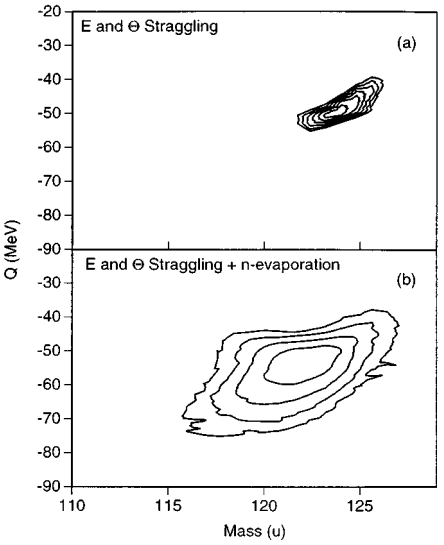

FIG. 5. The effects of energy straggling, small-angle scattering, and neutron evaporation on the measured mass and Q-value spectra are shown based on the Monte Carlo calculations described in the text. The initial distribution is assumed to be a δ function in both mass and Q. The effects of energy and angle straggling are to create a tail to larger masses and more positive Q values. Neutron evaporation moves the distribution to lower masses and more negative Q values and introduces considerable broadening in both parameters.

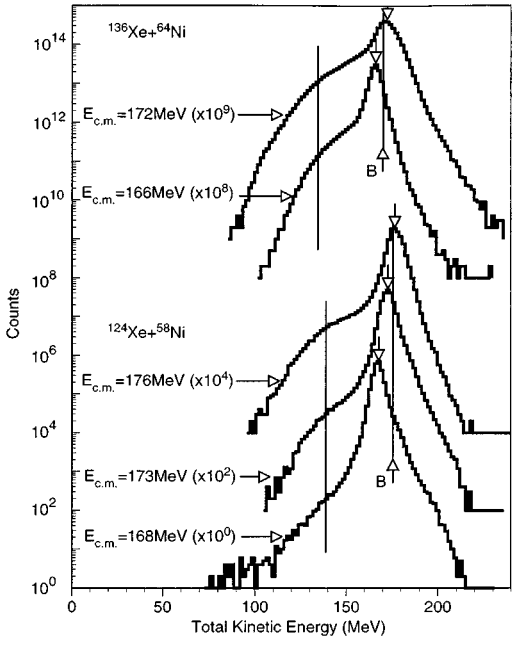

FIG. 6. Spectra of the total kinetic energy over the angular range covered in the measurements. Note that the spectra are not corrected for the geometric detection efficiency and represent only events with masses differing by less than 10 u from the entrance channel. The bombarding energies are indicated by the downward arrows, the Coulomb energies of touching spherical nuclei by the vertical lines with upward pointing arrows and letter B, and the Coulomb energy of two nuclei with deformation of 2:1 and touching end on by the vertical lines without arrows.

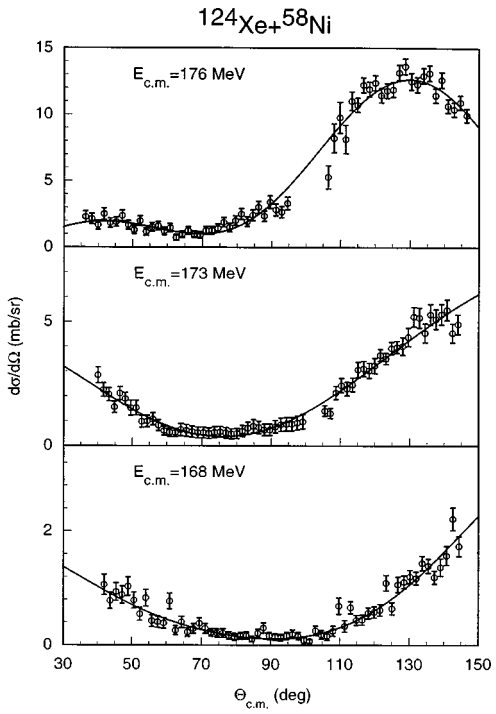

FIG. 7. Angular distributions for deep-inelastic scattering for ^{124}Xe+ ^{58}Ni. The solid line represents the fit to a fourth-order polynomial in cos θ used to extract the total cross section.

in Fig. 6 for the two systems and five bombarding energies investigated. The position of the interaction barrier, B, is indicated in the figure. A lower limit to the TKE spectra of about 100 MeV is observed which is rather independent of the system and the bombarding energy. In all cases, this limit is not the result of the detector geometry or energy loss in the entrance foils of the detectors. The 1-μm Mylar foils used in the PGAC detectors allow the detection of Xe ions with a kinetic energy of as little as 10 MeV. The TKE spectra are seen to extend down to (and below) the expected range for fissionlike processes.

The size of the low-energy shoulder relative to the elastic +quasielastic peak diminishes dramatically with decreasing bombarding energy. The shoulder is clearly evident at the highest bombarding energies and is almost gone at the lowest energy in the system ^{124}Xe+ ^{58}Ni. However, even at incident energies below the barrier, there are processes where significant dissipation of the kinetic energy occurs. The observed lower limit to the shoulder corresponds to an energy 70–80 MeV below the Coulomb barrier in the entrance channel.

D. Angular distributions

In order to integrate the deep-inelastic cross section, we will include all reactions with a Q value more negative than −20 MeV and a mass within 10 u of projectile or target in the deep-inelastic scattering component [4]. This distinction is purely an empirical one, and some contributions to these reactions could result from the tail of the fission distribution as well.

Angular distributions for deep-inelastic scattering in ^{124}Xe+ ^{58}Ni are plotted in Fig. 7 for the three different bombarding energies. They show a bell-shaped component which moves to larger angles with decreasing bombarding energy

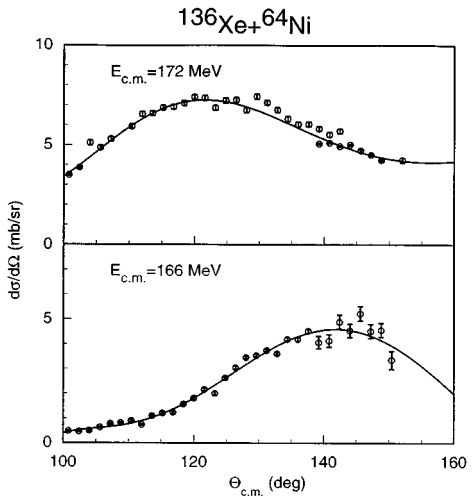

FIG. 8. Angular distributions for deep-inelastic scattering for ^{136}Xe+^{64}Ni. The solid line represents the fit to a fourth-order polynomial in cos θ used to extract the total cross section.

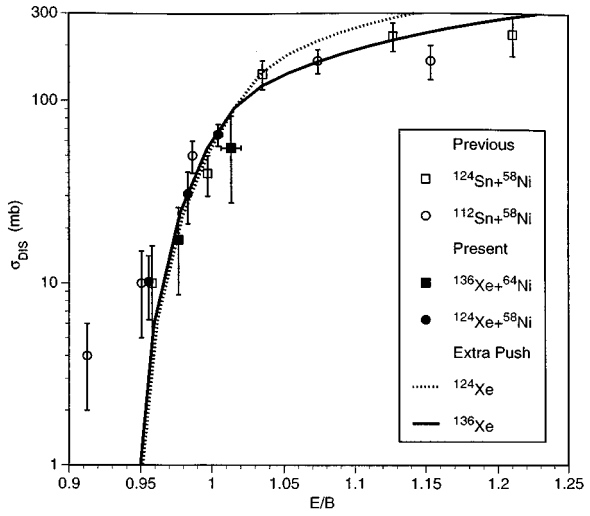

FIG. 9. Total cross sections for deep-inelastic scattering combined with the measurements of Wolfs [4] as a function of bombarding energy relative to the Coulomb barrier.

together with a forward-rising component, such that at the lowest energies the angular distribution becomes more symmetric around 90°. The ^{136}Xe date are illustrated in Fig. 8. Because of the detector geometry and target effects (see Sec. II), deep-inelastic scattering could not be separated from quasielastic and elastic scattering at forward angles in the ^{136}Xe measurement. This is the reason that for this case only the data at backward angles are shown.

E. Deep-inelastic scattering cross sections

Total cross sections for deep-inelastic scattering were extracted from the angular distribution by fitting with a fourth-order polynomial in the cosine of the scattering angle and integrating the fitted curves. The total cross sections are listed in Table II and plotted in Fig. 9 versus the bombarding energy divided by the Coulomb barrier energy [calculated using the equation $B=Z_1Z_2e^2/r_0(A_1^{1/3}+A_2^{1/3})$, where $r_0=1.4$ fm]. The forward angle contribution for ^{136}Xe+^{64}Ni was estimated from the measured backward angle cross section and a linear interpolation of the ratio of the forward and backward contributions in ^{124}Xe+^{58}Ni as a function of the center-of-mass energy divided by the Coulomb barrier energy. This is an empirical procedure to extrapolate into the unobserved region. The angular distribution in the observed region did not require any additional terms in the fitting procedure.

TABLE II. Total cross sections for deep-inelastic scattering.

System	$E_{\rm c.m.}$ (MeV)	E/B	$\sigma_{\rm dis}$ (mb)	$\sigma_{\theta>90°}$ (mb)	$\sigma_{\theta<90°}$ (mb)
^{124}Xe	176.4±0.4	1.005(3)	65±9	56±8	9.5±1.1
^{124}Xe	172.7±0.4	0.984(2)	31±10	22±6	9±4
^{124}Xe	167.8±0.4	0.956(2)	10±4	6±3	4.1±1.5
^{136}Xe	172.4±1.1	1.013(7)	55±28[a,b]	52±20[b]	
^{136}Xe	166.2±0.5	0.977(3)	17±9[a]	12±2	

[a]Includes uncertainty in estimated forward angle contribution (see text).

[b]Corrected for thick target (see text).

The uncertainty in the measured cross section is due to statistical uncertainties in the data, uncertainties in the extrapolation of the fit to forward and backward angles, and uncertainties in the overall normalization. Statistical uncertainties are included in the fitting procedure. For the ^{124}Xe data, the uncertainty in the extrapolation to angles where there is no experimental data is taken to be one-half of the contribution to the cross section from these angles. The uncertainty in the overall normalization is estimated to be 10%. All of these uncertainties are added in quadrature to arrive at the values listed in Table II. For the ^{136}Xe data, the uncertainty in the backward angle cross section is calculated similarly to ^{124}Xe. The uncertainty in the total cross section is taken to be one-half of its magnitude, in order to account for the uncertainty in the estimate of the forward angle contribution.

The ^{136}Xe high-energy cross section was measured with a thick target 397μg/cm^2 and was corrected for the effect of the energy loss in the target material combined with the exponential energy dependence below the barrier. This correction was performed by fitting an exponential function of the energy over the barrier to the other Xe data points and then integrating this function to derive an effective target thickness for the measurement. This correction increases the measured cross section by a factor of 1.6 for this energy. Similar corrections were negligible for the other measurements performed with thin targets ($<$100 μg/cm^2) and were not included.

The deep-inelastic cross sections of Ref. [4] are included in Fig. 9 for comparison (open symbols). We observe that the deep-inelastic cross section in all of the measured systems is similar at energies below the barrier.

F. Comparison to the extra push model

It is of interest to compare the present data to the predictions of the extra push model. In this model, deep-inelastic collisions are associated with events where the system proceeds behind the interaction barrier, but fails to surpass the conditional saddle ridge. For this comparison we use a modi-

fied version of the extra push model [11], where the liquid drop model surface tension γ and the nuclear radius parameter r_0 are taken from Ref. [12]. These values, when used to compute interaction barrier with the proximity potential Ref. [13], give good overall agreement with experimental data. The model has furthermore been modified to include the effects of target deformation or zero-point vibrations [14], and the parameters for the extra push energy have been adjusted to account for a large set of data on quasifission and complete fusion cross sections [15]. Calculations using this model are compared to the measured deep-inelastic cross section in Fig. 9. The data are reproduced quite well by the calculations, including the observed deep-inelastic cross section at subbarrier energies. It is interesting to note that this macroscopic model reproduces both sets of data equally well, pointing to the conclusion that the difference in nuclear structure between ^{124}Xe and ^{136}Xe does not seem to significantly affect the deep-inelastic cross section.

IV. CONCLUSIONS

With few exceptions [4], studies of deep-inelastic scattering of heavy projectiles have traditionally been carried out at beam energies substantially higher than the Coulomb barrier, where this reaction channel constitutes a larger fraction of the total reaction strength. In the present study, we have shown that the deep-inelastic scattering process plays a significant role also at subbarrier energies, despite the fact that at the distance of closest approach the relative motion is effectively eliminated in the entrance channel. The most negative Q values observed correspond to total kinetic energies characteristic of fission processes.

The main motivation for this work was to identify possible effects of the differences in nuclear structure of the two projectiles ^{124}Xe and ^{136}Xe on the deep-inelastic cross section. Such effects are expected to be larger below the barrier as a result of lower excitation energies of the final state nuclei. In a comparison of the two systems where the trivial Coulomb-barrier effect has been removed, as well as in a comparison of the data with the prediction of the macroscopic extra push model, we do not observe any effect, within experimental uncertainty, that can be attributed to the difference in nuclear structure. We find also that the deep-inelastic cross section, even at subbarrier energies, is well described by the modified extra push model.

ACKNOWLEDGMENTS

We wish to thank the ATLAS operations staff for providing excellent Xe beams for these experiments. One of us (J.G.) would like to acknowledge that this work was performed at Argonne National Laboratory under a program administered by the Argonne Division of Educational Programs with funding from the U.S. Department of Energy. This paper was presented as a thesis to the Department of Physics, The University of Chicago, in partial fulfillment of the requirements for a Ph.D. degree. This work was supported by the U.S. Department of Energy under Contract No. W-31-109-ENG-38.

[1] A. G. Artukh, G. F. Gridnev, V. L. Mikheev, V. V. Volkov, and J. Wilczynski, Nucl. Phys. **A215**, 91 (1973).
[2] M. Lefort, C. Ngô, J. Péter, and B. Tamain, Nucl. Phys. **A216**, 166 (1973).
[3] K. L. Wolf, J. P. Unik, J. R. Huizenga, J. Birkelund, H. Freiesleben, and V. E. Viola, Phys. Rev. Lett. **33**, 1105 (1974).
[4] F. L. H. Wolfs, Phys. Rev. C **36**, 1379 (1987).
[5] M. Beckermann, Rep. Prog. Phys. **51**, 1047 (1988), and references therein.
[6] K. E. Rehm, M. Paul, J. Gehring, B. Glagola, D. Henderson, W. Kutschera, and A. H. Wuosmaa, Nucl. Instrum. Methods Phys. Res. A **344**, 614 (1994).
[7] R. Pardo, B. E. Clifft, P. Denhartog, D. Kovar, W. Kutschera, and K. E. Rehm, Nucl. Instrum. Methods Phys. Res. A **270**, 226 (1988).
[8] J. F. Ziegler, *The Stopping and Ranges of Ions in Matter* (Pergamon, New York, 1977).
[9] V. E. Viola, K. Kwiatkowski, and G. Walker, Phys. Rev. C **31**, 1550 (1985).
[10] A. Gavron, Phys. Rev. C **21**, 230 (1980).
[11] J. Tõke, R. Bock, G. X. Dai, A. Gobbi, S. Gralla, K. D. Hildenbrand, J. Kuzminski, W. F. J. Müller, A. Olmi, H. Stelzer, B. B. Back, and S. Bjørnholm, Nucl. Phys. **A440**, 327 (1985).
[12] P. Möller and J. R. Nix, At. Data Nucl. Data Tables **26**, 165 (1981).
[13] J. Blocki, J. Randrup, W. J. Swiatecki, and C. F. Tsang, Ann. Phys. (N.Y.) **105**, 477 (1977).
[14] B. B. Back, R. R. Betts, J. E. Gindler, B. D. Wilkins, S. Saini, M. B. Tsang, G. K. Gelbke, W. G. Lynch, M. A. McMahan, and P. A. Baisden, Phys. Rev. C **32**, 195 (1985).
[15] W. Q. Shen, J. Albinski, A. Gobbi, S. Gralla, K. D. Hildenbrand, N. Herrmann, J. Kuzminski, W. F. J. Müller, H. Stelzer, J. Tõke, B. B. Back, S. Bjørnholm, and S. P. Sørensen, Phys. Rev. **36**, 115 (1987).